

Mass loss from the exoplanet WASP-12b inferred from *Spitzer* phase curves

Taylor J. Bell¹,¹ Michael Zhang,² Patricio E. Cubillos,³ Lisa Dang,¹ Luca Fossati,³ Kamen O. Todorov,⁴ Nicolas B. Cowan,^{1,5} Drake Deming,⁶ Robert T. Zellem,⁷ Kevin B. Stevenson,⁸ Ian J. M. Crossfield,⁹ Ian Dobbs-Dixon,¹⁰ Jonathan J. Fortney,¹¹ Heather A. Knutson¹² and Michael R. Line¹³

¹Department of Physics, McGill University, 3600 rue University, Montréal, QC H3A 2T8, Canada

²Department of Astronomy, California Institute of Technology, 1216 E California Blvd, Pasadena, CA 91125, USA

³Space Research Institute, Austrian Academy of Sciences, Schmiedlstrasse 6, A-8042 Graz, Austria

⁴Anton Pannekoek Institute for Astronomy, University of Amsterdam, Science Park 904, NL-1090 GE Amsterdam, The Netherlands

⁵Department of Earth and Planetary Sciences, McGill University, 3450 rue University, Montréal, QC H3A 0E8, Canada

⁶Department of Astronomy, University of Maryland, College Park, MD 20742, USA

⁷Jet Propulsion Laboratory, California Institute of Technology, 4800 Oak Grove Drive, Pasadena, CA 91109, USA

⁸Space Telescope Science Institute, Baltimore, MD 21218, USA

⁹Department of Physics, Massachusetts Institute of Technology, Cambridge, MA 02139, USA

¹⁰Department of Physics, NYU Abu Dhabi, PO Box 129188, Abu Dhabi, UAE

¹¹Other Worlds Laboratory, Department of Astronomy and Astrophysics, University of California, Santa Cruz, CA 95064, USA

¹²Division of Geological and Planetary Sciences, California Institute of Technology, Pasadena, CA 91125, USA

¹³School of Earth and Space Exploration, Arizona State University, Tempe AZ 85287, USA

Accepted 2019 July 17. Received 2019 July 16; in original form 2019 June 6

ABSTRACT

The exoplanet WASP-12b is the prototype for the emerging class of ultrahot, Jupiter-mass exoplanets. Past models have predicted – and near-ultraviolet observations have shown – that this planet is losing mass. We present an analysis of two sets of 3.6 and 4.5 μm *Spitzer* phase curve observations of the system which show clear evidence of infrared radiation from gas stripped from the planet, and the gas appears to be flowing directly toward or away from the host star. This accretion signature is only seen at 4.5 μm , not at 3.6 μm , which is indicative either of CO emission at the longer wavelength or blackbody emission from cool, $\lesssim 600$ K gas. It is unclear why WASP-12b is the only ultrahot Jupiter to exhibit this mass-loss signature, but perhaps WASP-12b's orbit is decaying as some have claimed, while the orbits of other exoplanets may be more stable; alternatively, the high-energy irradiation from WASP-12A may be stronger than the other host stars. We also find evidence for phase offset variability at the level of 6.4σ (46.2°) at 3.6 μm .

Key words: accretion, accretion discs – techniques: photometric – planets and satellites: individual (WASP-12b) – planet–star interactions.

1 INTRODUCTION

The exoplanet WASP-12b (Hebb et al. 2009) is one of the hottest planets known to date and, as a result of its exceedingly tight orbit and inflated radius ($a/R_* = 3.039$, $R_p = 1.900 R_J$; Collins, Kielkopf & Stassun 2017), it is one of the best-studied exoplanets. WASP-12b is also the archetype of an emerging class of exoplanets called ultrahot Jupiters (UHJs). Planets in this regime are so strongly

irradiated by their host star that many of the molecules (e.g. H_2 and H_2O) in their dayside atmospheres thermally dissociate (Bell et al. 2017; Bell & Cowan 2018; Arcangeli et al. 2018; Kreidberg et al. 2018; Lothringer, Barman & Koskinen 2018; Mansfield et al. 2018; Parmentier et al. 2018) and may recombine nearer the nightside (Bell & Cowan 2018; Komacek & Tan 2018; Parmentier et al. 2018). UHJs also bear some similarities to cataclysmic variable star (CV) systems and may undergo significant tidal distortion and mass loss, depending on the specifics of the star–planet system (e.g. Bisikalo et al. 2013a; Burton et al. 2014).

* E-mail: taylor.bell@mail.mcgill.ca

While tidal distortion is expected for WASP-12b, a 2010 *Spitzer* Infrared Array Camera (IRAC) thermal phase curve observation of WASP-12b at 4.5 μm demonstrated second-order sinusoidal variations (with two maxima per planetary orbit) that were far greater than predicted (Cowan et al. 2012). The substellar axis would have to be 1.8 times as long as the dawn–dusk and polar axes if the observed variations were entirely due to the tidally distorted shape of the planet. Additionally, no evidence of these second-order sinusoidal variations was found in a *Spitzer*/IRAC 3.6 μm phase curve also taken in 2010 (Cowan et al. 2012).

In this paper, we combine a new set of phase curves taken in 2013 with a re-analysis of the data from 2010 to determine the source of the unusually strong second-order sinusoidal variations at 4.5 μm reported by Cowan et al. (2012). The observations are described in Section 2. Our three astrophysical models are described in Section 3.1, and our three independent reduction and decorrelation methods are described in Section 3.2. Results and their physical implications are presented in Section 4, and Section 5 contains the discussion and conclusion.

2 OBSERVATIONS

We combine two sets of two-channel (3.6 and 4.5 μm) *Spitzer*/IRAC observations taken in 2010 (PID 70060, PI: Machalek) and 2013 (PID 90186, PI: Todorov), all during the Post-Cryogenic *Spitzer* Mission. In all four phase curves, the system was observed nearly continuously for ~ 33 h (breaking only once or twice to repoint the telescope), beginning shortly before one secondary eclipse and ending shortly after the subsequent secondary eclipse. The reduced and detrended observations are shown in Fig. 1.

For both data sets, the subarray mode was used with 2 s exposures which produced data cubes of 64 images with 32×32 pixel ($39 \text{ arcsec} \times 39 \text{ arcsec}$) dimensions. The 2010 observations were divided into two Astronomical Observation Requests (AORs) with a total of 902 data cubes (57 728 exposures), while the 2013 observations were divided into 3 AORs with a total of 909 data cubes (58 176 exposures). The 2010 full-phase observations were published by Cowan et al. (2012), the eclipse timings from the 2013 observations were published by Patra et al. (2017), and some derived parameters from all four phase curves were published as part of a broad comparison between different planets (Zhang et al. 2018).

Past observations of WASP-12 show a nearby M-dwarf binary system WASP-12B,C 1.06 arcsec away from WASP-12A (Bergfors et al. 2011; Crossfield et al. 2012b; Bechter et al. 2014). As this binary system lies too close to WASP-12A to be resolved by *Spitzer*, we correct for blended light after analysing the light curves, following past work (Stevenson et al. 2014a); see Appendix A for more details.

3 LIGHT-CURVE ANALYSIS

3.1 Astrophysical models

We model the observations as

$$F_{\text{model}}(t) = A(t) \times \tilde{D}(t)$$

where $\tilde{D}(t)$ is the normalized detector model; see Section 3.2 for details on the specific models used which consist of both parametric (2D polynomials and pixel level decorrelation) and non-parametric models (bilinear interpolated subpixel sensitivity mapping). The

astrophysical model is

$$A(t) = F_*(t) + F_p(t),$$

where F_* is the flux from the host star (assumed to be constant except during transits) and F_p is the planetary flux. Transits and eclipses are modelled using BATMAN (Kreidberg 2015), assuming a quadratic limb-darkening model for the host star and a uniform disc for the planet. The planetary flux is modelled as

$$F_p(t) = F_{\text{day}} \Phi(\psi(t)),$$

where F_{day} is the instantaneous eclipse depth at phase 0.5 (assumed to be constant over each ~ 33 h phase curve), Φ describes the phase variations, and the orbital phase with respect to eclipse is $\psi(t) = 2\pi(t - t_e)/P$, where t_e is the time of eclipse and P is the planet's orbital period.

We consider three different models for the astrophysical phase variations in the light curve. The simplest astrophysical model we consider is a first-order sinusoid

$$\Phi_1(\psi) = 1 + C_1 \left(\cos(\psi) - 1 \right) + D_1 \sin(\psi),$$

and we also consider a second-order sinusoid

$$\Phi_2(\psi) = \Phi_1(\psi) + C_2 \left(\cos(2\psi) - 1 \right) + D_2 \sin(2\psi),$$

where $C_1, D_1, C_2,$ and D_2 are all constants. If the previously reported double-peaked phase curve (Cowan et al. 2012) is astrophysical in nature, one potential interpretation is that some/all of the power in the second-order sinusoidal variations is from tidal distortion of the planet. We model this scenario with

$$\Phi_{1,\text{ellipsoid}}(\psi) = S(\psi)\Phi_1(\psi),$$

where $S(\psi)$ describes the projected area of an ellipsoid as it rotates. Rather than model a triaxial ellipsoid, we constrain the polar and dawn–dusk axes to share the same length since rotational deformation is expected to be negligible compared to tidal deformation (Leconte, Lai & Chabrier 2011a). To find the deviations in the projected area of this biaxial ellipsoid, we adapt an equation from past work (Leconte, Lai & Chabrier 2011b),

$$S(\psi) = \left[\sin^2(i) \left(\left(\frac{R_{p,2}}{R_p} \right)^2 \sin^2(\psi) + \cos^2(\psi) \right) + \left(\frac{R_{p,2}}{R_p} \right)^2 \cos^2(i) \right]^{1/2},$$

where i is the orbital inclination, R_p is the planetary radius along the polar and dawn–dusk axes (the two axes observed during transit and eclipse if $i = 90^\circ$), and $R_{p,2}$ is the planetary radius along the line connecting the planet and star (the substellar axis).

3.2 Decorrelation procedures

To ensure our results are robust and independent of the methods used, we perform three independent reductions and analyses following previously employed methods (Cubillos et al. 2014; Dang et al. 2018; Zhang et al. 2018) which are summarized below. Each analysis considers all three phase variation models. The model priors for each analysis are described below and summarized in Table A1 for convenience. Within each analysis pipeline, models are selected based on the Bayesian Information Criterion (BIC). We cannot choose our fiducial models between our three analyses using the BIC as there are significant differences between the

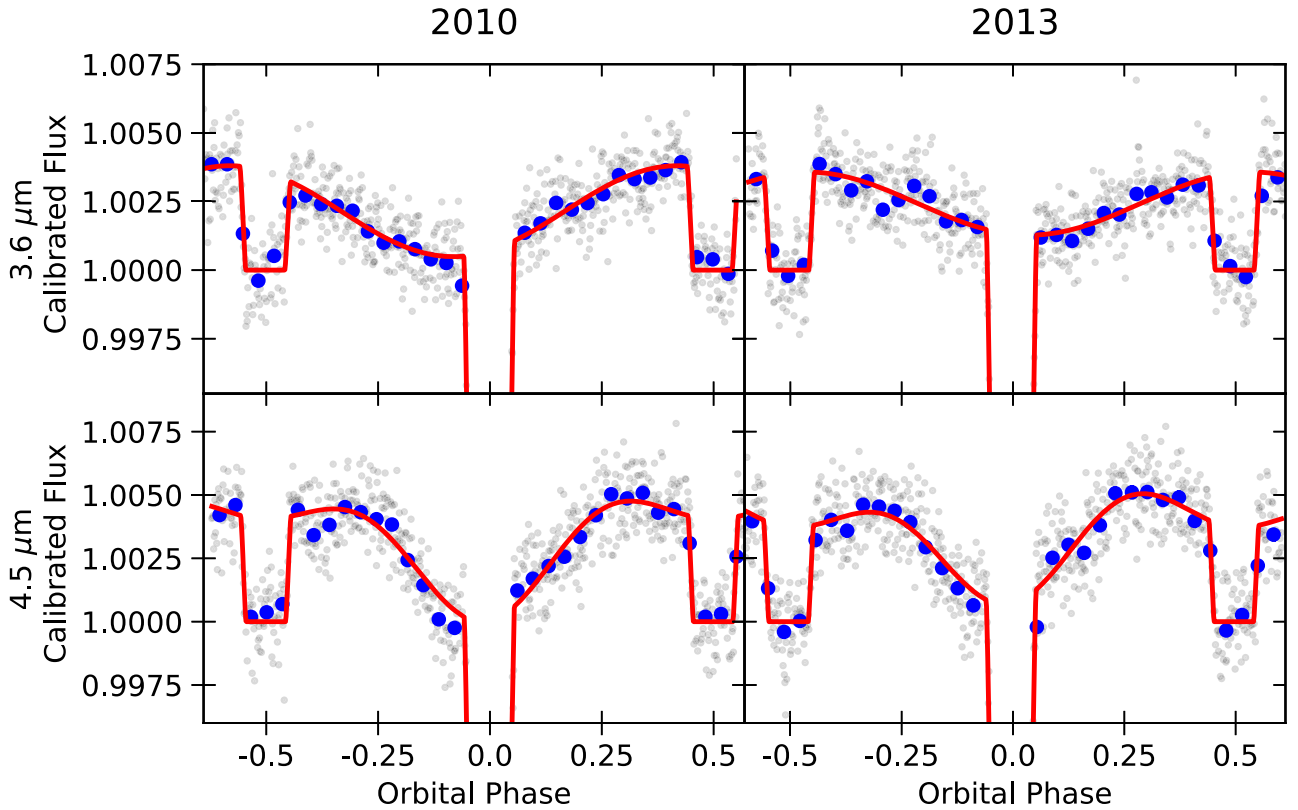


Figure 1. Fiducial analyses of 3.6 μm (top) and 4.5 μm (bottom) *Spitzer*/IRAC phase curve observations of WASP-12b taken in 2010 (left) and 2013 (right). Both 3.6 μm phase curves show one maximum per planetary orbit, while both 4.5 μm phase curves exhibit two maxima per planetary orbit. The detector systematics have been removed from the data, and our fiducial astrophysical models for each data set are overplotted in red. Grey data points show binned values from each *Spitzer* data cube (64 frames), and the blue points show more coarsely binned values (1664 frames).

number of data used in each analysis because of different σ -clipping and binning. Instead, we choose to discriminate between the three analyses by selecting the model with the largest log-likelihood per datum, $\ln(L)/N_{\text{data}}$; we therefore adopt the preferred models from M. Zhang’s analyses as our fiducial models. The fiducial reductions of the four data sets are presented in Fig. 1 and Table 1 (see also Table A1, Figs A5 and A6, and Supporting Information).

3.2.1 Fiducial reduction and decorrelation procedure

For reasons described below, M. Zhang’s analyses were selected as our fiducial analyses and follow their previous work (Zhang et al. 2018). In this analysis, we perform aperture photometry with a radius of 2.7 pixels on the *Spitzer* Basic Calibrated Data (BCD) files to get the raw flux for all frames. The background is calculated by excluding all pixels within a radius of 12 pixels from the star, rejecting outliers using σ -clipping, and then calculating the biweight location of the remaining pixels. We then bin the background-subtracted raw fluxes with a bin size of 64, discard the first 0.05 days of data, and perform fitting with EMCEE (Foreman-Mackey et al. 2013). The fitting uses 250 walkers that walk for 20 000 burn-in steps and 20 000 post-burn-in steps. Our instrumental model uses first-order pixel level decorrelation (PLD) for all data except the 2010 3.6 μm data, in which case we find that second-order PLD minimizes BIC. Aside from PLD, the instrumental model also includes a linear slope with respect to time. We fit for the following parameters, all with uniform priors: transit time, eclipse time, R_p/R_* , eclipse depth (assumed to be constant over each ~ 33 h

phase curve), sinusoidal phase variation amplitudes (C_1 and D_1 for the first-order sinusoid, and C_2 and D_2 if running a second-order sinusoidal model), photometric error, slope in flux with time, and PLD coefficients. We fixed P , a/R_* , and i to the highly precise values from the literature (Collins et al. 2017) as they are poorly constrained by our observations. As limb darkening is not that important in the *Spitzer* bands, we adopt the closest model from a grid of 1D stellar models (Sing 2010).

Our fiducial analyses find that the photon noise limits are 652 and 637 ppm for the 2010 and 2013 3.6 μm observations, respectively, and the limits for the 2010 and 2013 4.5 μm observations are 866 and 860 ppm, respectively. The differences between these two is likely due to the star falling on parts of the detector with slightly different sensitivities, as well as varying aperture sizes. The fitted photometric standard deviation from our fiducial analyses are 950 and 976 ppm for the 2010 and 2013 3.6 μm observations (1.46 and 1.53 times greater than the photon noise limit). For the 2010 and 2013 4.5 μm observations, the fitted photometric standard deviations are 1134 and 1158 ppm (1.31 and 1.35 times greater than the photon noise limit). The normalized raw, decorrelated, and residual fluxes from all four phase curves analysed with M. Zhang’s pipeline are presented in Figs A5 and A6.

3.2.2 T. Bell’s reduction and decorrelation procedure

Reduction and decorrelation of these data follow Dang et al. (2018) and are summarized here. We convert the pixel intensity from MJy str^{-1} to electron counts and mask bad pixels, i.e. 4σ outliers

Table 1. Key fiducial light-curve parameters.

Data set	R_p/R_* ^b	First-order phase offset ^a (deg)	Second-order phase offset ^a (deg)	F_{day}/F_* ^b (ppm)
2010, 3.6 μm	0.11642 ± 0.00063	-32.6 ± 6.2	–	3870 ± 130
2013, 3.6 μm	0.11327 ± 0.00068	13.6 ± 3.8	–	3840 ± 120
2010, 4.5 μm	0.10656 ± 0.00085	-9.5 ± 2.3	94.7 ± 1.6	4360 ± 140
2013, 4.5 μm	0.1049 ± 0.0010	-19.1 ± 3.9	93.2 ± 1.9	3920 ± 150

Notes: ^aThese phase offsets are measured in degrees *after* eclipse and are derived quantities.

^bThese quantities have been corrected for dilution from WASP-12BC (see Appendix A).

with respect to the median of that pixel in the data cube as well as any NaN pixels. We discard all frames with a bad pixel within the aperture used for photometry. We also discard every first frame from each data cube from the 2010 observations and every first and second frame from each data cube for the 2013 observations because these frames consistently show the presence of significant outliers compared to other frames within the same data cube. The effect of this σ -clipping is minimal, given that model fitting is performed on the median binned values from each data cube. There is another star (other than WASP-12A,B,C) that falls on the detector but lies outside the considered photometric apertures (~ 10 arcsec away); we place a 3×3 pixel mask around this star to ensure that it does not bias the background subtraction.

We then perform aperture photometry on each individual frame, with an aperture at the fixed pixel-location (15,15), and centroids were found using a flux-weighted mean algorithm and later used for decorrelation. Apertures ranging from 2 to 5 pixels in radius were considered as well as two different aperture edges: hard (the pixel’s flux is included if the centre of the pixel lies within the aperture) and soft (each pixel is weighed by the exact fraction of its area included within the aperture). While some flux will be lost by smaller apertures, a smaller aperture better allows us to remove intrapixel sensitivity variations, which are the dominant source of noise in our data. We select the aperture radius and edge which resulted in the lowest rms after a copy of the raw data were smoothed by a boxcar filter of width 5 data cubes (~ 11 min which is approximately half the ingress/egress duration) to remove features such as transits, eclipses, and phase variations. Tests run with apertures centred on the flux-weighted mean derived centroids showed that the rms was >100 ppm higher than the fixed position apertures. For the 2010 data, we selected a hard-edged 2.5 pixel radius aperture for the 4.5 μm data and a soft-edged 4.3 pixel radius aperture for the 3.6 μm data; the previous analysis of these data (Cowan et al. 2012) used IDL’s approximation on a soft-edged 2.5 pixel radius aperture for both wavelengths. For the 2013 data, we selected a hard-edged 3.2 pixel radius aperture for the 4.5 μm data and a soft-edged 2.9 pixel radius aperture for the 3.6 μm data. Before decorrelating and analysing the data, we first bin the flux and centroid measurements from all 64 frames within a data cube using a median to reduce noise and decrease computation time. On average, each of our models take ~ 0.5 h to fit to the binned data, and computation time grows linearly with the number of data points, so running each of the different models on unbinned data is not feasible.

T. Bell’s analyses used various systematic models as implemented in the open-source Spitzer Phase Curve Analysis (SPCA; Dang et al. 2018) pipeline.¹ In particular, we used 2D polynomials of

order 2–5 and BiLinear Interpolated Subpixel Sensitivity (BLISS) mapping. The 2D polynomials (Charbonneau et al. 2008) assume the sensitivity of the detector can be described by an n th-order 2D polynomial in the measured centroid. BLISS mapping (Stevenson et al. 2012a; Ingalls et al. 2016; Schwartz & Cowan 2017) is a non-parametric method to account for the intrapixel sensitivity variations which requires accurate centroid measurements; when fitting BLISS models we adopt an 8×8 grid of knots. For the 2013 observations at 3.6 μm , we also needed to add a slope in time to remove residual red noise.

Models were fit using the Markov Chain Ensemble Sampler EMCEE (Foreman-Mackey et al. 2013). The orbital parameters of WASP-12b in the literature (Collins et al. 2017) have smaller errors than we can achieve with our photometry. Additionally, numerous searches for eccentricity have found that WASP-12b’s orbit is best described by a circular orbit (Campo et al. 2011; Croll et al. 2011; Bailey & Goodman 2019), so we set the orbital eccentricity to zero. Several orbital parameters are poorly constrained by a single-phase curve observation compared to the literature values, so we adopted the following Gaussian priors to marginalize over the uncertainties in the literature values: $t_0 = 56176.16825800 \pm 0.00007765$ (BJD), $a/R_* = 3.039 \pm 0.034$, $i = 83.37^\circ \pm 0.68^\circ$ (Collins et al. 2017). The orbital period is known to within 12 ms, so we simply fixed it at 1.09142030 d (Collins et al. 2017). The parameters that were always fitted were t_0 , R_p/R_* , a/R_* , i , F_{day}/F_* , two quadratic limb-darkening parameters (Kipping 2013) q_1 and q_2 , and the first-order sinusoidal amplitudes C_1 and D_1 . In some models, we also fitted $R_{p,2}/R_*$ or C_2 and D_2 . A number of detector parameters were also fitted, with the exact number depending on the detector model used.

For T. Bell’s apertures, the photon noise limits are 578 and 566 ppm for the 2010 and 2013 3.6 μm observations, respectively, and the limits for the 2010 and 2013 4.5 μm observations are 795 and 791 ppm, respectively. The fitted photometric standard deviation from T. Bell’s analysis are 1493 and 1246 ppm for the 2010 and 2013 3.6 μm observations (2.58 and 2.20 times greater than the photon noise limit). For the 2010 and 2013 4.5 μm observations, the fitted photometric standard deviations are both 1440 ppm (1.81 and 1.82 times greater than the photon noise limit). The fitted data and red noise tests from these analyses can be found in the Supporting Information (Figs A7 and A8).

3.2.3 P. Cubillos’ reduction and decorrelation procedure

The models run by P. Cubillos use the Photometry for Orbits, Eclipses, and Transits (POET) pipeline (Stevenson et al. 2010; Campo et al. 2011; Nymeyer et al. 2011; Stevenson et al. 2012a,b; Cubillos et al. 2013, 2014). The POET pipeline starts by flagging bad pixels from the *Spitzer* BCD files using the permanent bad

¹<https://github.com/lisadang27/SPCA>

pixel masks and performing a sigma-rejection routine. Next, it estimates the target centre position either fitting a 2D Gaussian function or calculating the least asymmetry (Lust et al. 2014). Then, it obtains raw light curves by applying a circular interpolated aperture photometry, testing several aperture radii between 2.0 and 4.0 pixels.

To determine the optimal centroiding method and photometry aperture, POET minimizes the standard deviation of the residuals, and minimizes time-correlated noise at time-scales equal and larger than the transit duration (estimated through the time-averaging method). Least asymmetry centroiding outperformed Gaussian centring for all data sets, except the 2013 4.5 μm observation. The optimal apertures were 2.5 and 3.0 pixels (2010) and 4.0 and 2.0 pixels (2013) for the 3.6 and 4.5 μm observations, respectively. In any case, all relevant astrophysical parameters vary within their uncertainties as we vary the centroiding and photometry.

POET models the unbinned light curves, simultaneously fitting the astrophysical phase curve and the telescope systematics. The systematics model consists of the non-parametric BLISS intrapixel model, for which we set the map's bin size equal to the rms of the frame-to-frame target position (0.01 pixels), and require at least 8 points per bin. For the 2013 4.5 μm observation, we also apply a linear time-dependent ramp with the slope as a free parameter.

The astrophysical model consists of transit and eclipse models (Mandel & Agol 2002), combined with the sinusoidal and ellipsoid models described in the Methods section. The transit free fitting parameters are the epoch, ratio between the planetary and stellar radii, cosine of inclination, semimajor axis to stellar radius ratio, stellar flux, and quadratic limb-darkening coefficients. The eclipse-free fitting parameters are the mid-point, duration, depth, and ingress duration (setting the egress duration equal to the ingress duration). We adopt uniform priors for all parameters, except for $\cos(i)$ and a/R_* , which have Gaussian priors, and kept the orbital period fixed (same values as in T. Bell's reduction and decorrelation procedure; Collins et al. 2017).

POET incorporates the Multi-Core Markov-Chain Monte Carlo (MC3) statistical package (Cubillos et al. 2017) to find the best-fitting parameter values (using Levenberg–Marquardt optimization) and uncertainties (using a differential-evolution Markov Chain Monte Carlo algorithm; ter Braak & Vrugt 2008), requiring the Gelman–Rubin statistic (Gelman & Rubin 1992) to be within 1 per cent of unity for each free parameter for convergence. POET uses Bayesian hypothesis testing to select the model best supported by the data, selecting the lowest BIC model. The POET results support the independent results of the other pipelines. Both 4.5 μm observations strongly favour the second-order sinusoidal model, while both 3.6 μm observations strongly favour the first-order sinusoidal model.

For P. Cubillos' apertures, the photon noise limits are 4886 and 6664 ppm for the 2010 and 2013 3.6 μm observations, respectively, and the limits for the 2010 and 2013 4.5 μm observations are 8273 and 7988 ppm, respectively. The fitted photometric standard deviation from P. Cubillos' analysis are 6915 and 7360 ppm for the 2010 and 2013 3.6 μm observations (1.41 and 1.10 times greater than the photon noise limit). For the 2010 and 2013 4.5 μm observations, the fitted photometric standard deviations are 9130 and 8658 ppm (1.10 and 1.08 times greater than the photon noise limit). The fitted data and red noise tests from these analyses can be found in the Supporting Information (Figs A9 and A10).

4 RESULTS

4.1 Comparison between pipelines and epochs

All three independent analyses confirm the presence of strong and persistent second-order sinusoidal variations at 4.5 μm and the non-detection of these variations at 3.6 μm . The fitted phase curves parameters for the preferred models from all three independent pipelines are summarized in Fig. 1 and Table A2. See the Supporting Information for tabulated values for all considered models. The astrophysical parameters at 3.6 and 4.5 μm are mostly consistent between all three analyses, with the preferred models from the three analyses generally differing by $<2\sigma$. In the few cases where one model differs from the others by more than 2σ , the other two models are consistent with each other at a level of $<1\sigma$. Also, there is low-frequency noise in the 2010 4.5 μm residuals between the first eclipse and the end of the transit that is seen by all three analysis pipelines; the source of these variations is not understood.

From 2010 to 2013, the three pipelines show that all 4.5 μm phase curve and planetary parameters remain constant within $<2\sigma$. Most of the phase curve and planetary parameters at 3.6 μm also remain constant between the two observing epochs, with the main exception being the phase offset calculated using the first-order sinusoidal terms. M. Zhang's, P. Cubillos', and T. Bell's pipelines find that it changes by 6.4σ (46.2°), 7.7σ (46.6°), and 3.1σ (28.1°), respectively. All three pipelines also agree that the sign of the hotspot offset changes between the two observing epochs, with the offset being 'eastward' (before eclipse) in 2010 and 'westward' (after eclipse) in 2013. It is interesting to note, however, that over this same time span both the first- and second-order sinusoidal phase offsets from the 4.5 μm observations do not change. No other parameter is found by all three analyses to vary by more than 3σ between the two observing epochs. Finally, if the first-order sinusoidal phase variations are entirely attributable to WASP-12b's temperature map, our 2013 observations at 3.6 μm exhibit a 13.6 ± 3.8 westward hotspot offset. This may be a demonstration that eastward hotspot offsets are less ubiquitous than previously believed, with westward hotspot offsets reported for planets with irradiation temperatures spanning 2200–3700 K (Wong et al. 2016; Dang et al. 2018; Zhang et al. 2018).

4.2 Physical sources

The previously favoured explanation for the double-peaked phase curve reported for WASP-12b by Cowan et al. (2012) was detector systematics, but this hypothesis is now strongly disfavoured. To date, 23 papers have been published with new *Spitzer* phase curves of 18 different exoplanets (Harrington et al. 2006; Knutson et al. 2007; Cowan, Agol & Charbonneau 2007; Knutson et al. 2009a,b; Laughlin et al. 2009; Crossfield et al. 2010; Cowan et al. 2012; Knutson et al. 2012; Crossfield et al. 2012a; Lewis et al. 2013; Maxted et al. 2013; Zellem et al. 2014; Wong et al. 2015; de Wit et al. 2016; Wong et al. 2016; Krick et al. 2016; Demory et al. 2016; Wong et al. 2016; Stevenson et al. 2017; de Wit et al. 2017; Zhang et al. 2018; Dang et al. 2018; Kreidberg et al. 2018). Of these numerous observations, WASP-12 is the only system which has shown strong a double-peaked phase curve not once, but twice. The observing strategy also differed between these two sets of WASP-12b phase curves, with the number and timing of AORs changing and the addition of PCRS Peak-Up before the 2013 observations. The consistency between the two sets of phase curves suggests that

the observations probe an astrophysical source which does not vary significantly over a ~ 3 yr time-scale. Cowan et al. (2012) suggested that tidal distortion and/or mass loss might be able to explain the *Spitzer* observations, if this signal was indeed astrophysical in nature. We explore these and other potential sources of emission below.

4.2.1 Tidal distortion

One potential cause of second-order sinusoidal variations is tidal deformation of the host star, as is seen at optical wavelengths for HAT-P-7 (Welsh et al. 2010) and WASP-18 (Shporer et al. 2019). However, stellar distortion is expected to be negligible for WASP-12 (Leconte et al. 2011a). We verified this by numerically solving for the equipotential stellar/planetary surfaces using the dimensionless Roche potential (see Appendix C). However, since the star contributes significantly more flux than the planet, we ran simple simulations of both the star and planet including the effects of gravity darkening to assess their expected amplitudes of ellipsoidal variations. We find that the stellar ellipsoidal variations are approximately the same amplitude at 3.6 and 4.5 μm and the amplitude of the stellar variations are far smaller than the observed amplitudes; we therefore conclude that tidal bulges on the host star cannot be the source of the strong second-order variations observed at 4.5 μm . Our predicted ellipsoidal variations for WASP-12b are consistent with our limits on second-order sinusoidal variations at 3.6 μm , but significantly underpredict the observed amplitude at 4.5 μm (also see the implied dimensions of the best-fitting ellipsoidal variation model shown in the right-hand panel of Fig. 2). If we interpret the second-order sinusoidal variations at 4.5 μm as planetary ellipsoidal variations, this would require the 4.5 μm photosphere to be significantly higher up than 3.6 μm as the layers nearer the Roche lobe are more distorted. However, this increased radius at 4.5 μm is inconsistent with the smaller transit depth at 4.5 μm compared to 3.6 μm . We therefore conclude that tidal distortion of the planet is also not the source of the strong second-order variations observed at 4.5 μm .

4.2.2 Stellar variability and inhomogeneities

Stellar variability is also unlikely to be the cause of these observations given the comparable phase of the second-order variations in the two data sets. For reference, the WASP-12BC dilution correction term is ~ 400 ppm, while the observed amplitude of the second-order sinusoidal variations is ~ 2000 ppm. Additionally, variability in WASP-12A is only predicted to modulate the planetary signal at a level of ~ 1 ppm, and variability in WASP-12B,C should also only contribute at the level of ~ 1 ppm (while these M-dwarfs should be ~ 10 times more variable, they contribute ~ 10 times less flux; Zellem et al. 2017). We therefore rule out standard stellar variability as the source of the strong second-order sinusoidal variations seen at 4.5 μm . If the second-order variations were produced by unusually strong inhomogeneities on the host star, both the subplanet longitude and the antipoint longitude would need to be darker than intermediate longitudes – this would imply star–planet interactions. However, these inhomogeneities would also need to be much more pronounced at 4.5 μm which would not be expected for the ~ 6000 K star.

4.2.3 Mass loss

There is significant observational evidence from near-ultraviolet (NUV) transit observations that WASP-12b is undergoing mass loss and that there is a bow shock in the system (Fossati et al. 2010; Haswell et al. 2012; Nichols et al. 2015, see the Supporting Information). A potential explanation for the unusual 4.5 μm phase curve is that there is gas being stripped from the planet which emits more strongly within the 4.5 μm bandpass than the 3.6 μm bandpass. The observations favour a stream of dense gas stripped from the planet flowing directly toward/away from the host star or some other elongated patch of hot gas whose long axis is parallel to the star–planet axis, such as an accretion hot spot. Double-peaked phase curves have been seen for dwarf novae CVs, such as WZ Sge (Skidmore et al. 1997), however this feature was seen through the UV to infrared; for CVs these variations have been attributed to tidal distortion or an optically thick hotspot in an otherwise optically thin accretion disc (e.g. Skidmore et al. 1997).

The source of the 4.5 μm variations in the WASP-12 system must lie near the star–planet axis since there is no significant detection of an occultation of the source when the planet is not in transit or eclipse. Additionally, our *Spitzer* observations demonstrate that the planetary radius appears ~ 8 per cent (11σ) smaller at 4.5 μm than at 3.6 μm which is in disagreement with model predictions (Burrows et al. 2007; Burrows, Budaj & Hubeny 2008; Cowan et al. 2012); this rules out the transit of a large exosphere that is opaque at 4.5 μm as this would make the planetary radii at the two wavelengths even more discrepant.

As shown in Table 1, the fitted second-order offsets at 4.5 μm are consistent with being oriented along the star–planet axis (90°). However, previously published 3D magnetohydrodynamic (MHD) numerical simulations of hypothetical exoplanet systems mostly produced gas flows that significantly lead the star–planet axis (Matsakos, Uribe & Königl 2015). Indeed, gas streaming from the planet’s L1 Lagrange point on a ballistic trajectory should flow $\theta_{\text{gas}} = 53.4^\circ$ ahead of the star–planet axis (Lai et al. 2010) as angular momentum is conserved (see Fig. 2 for a schematic depiction). Assuming our observations probe the gas stream, this prediction is 27σ discrepant with our offset of 4.0 ± 2.1 behind the star–planet axis found by averaging the offsets from the two fitted second-order sinusoids at 4.5 μm . This discrepancy could potentially be explained if the 4.5 μm emitting area is much closer to the planet and is still aligned along the star–planet axis and then becomes more diffuse and flows ahead of the planet as it continues to fall toward the host star.

Alternatively, stellar effects could channel the infalling stream directly toward the star, but this may be inconsistent with past NUV transit observations (Fossati et al. 2010; Haswell et al. 2012; Nichols et al. 2015). One previously published 3D MHD model (Matsakos et al. 2015) did exhibit a stream of gas directly along the star–planet axis (their name for this model was ‘FvrB’). This model has high stellar UV flux, a low escape speed from the planet, the planet near to its host star, and a strong planetary magnetic field. In this model, the planet is experiencing Roche lobe overflow with a planetary wind that is weak compared to the stellar wind, producing an approximately linear stream of gas along the star–planet axis as well as a lower density tail trailing behind the planet (Matsakos et al. 2015). The non-detection of the gas trailing behind the planet could be explained if the gas has a lower density and/or has a lower temperature. As the dense gas stream in the ‘FvrB’ model is aligned along the star–planet axis, it may not contribute significantly to the

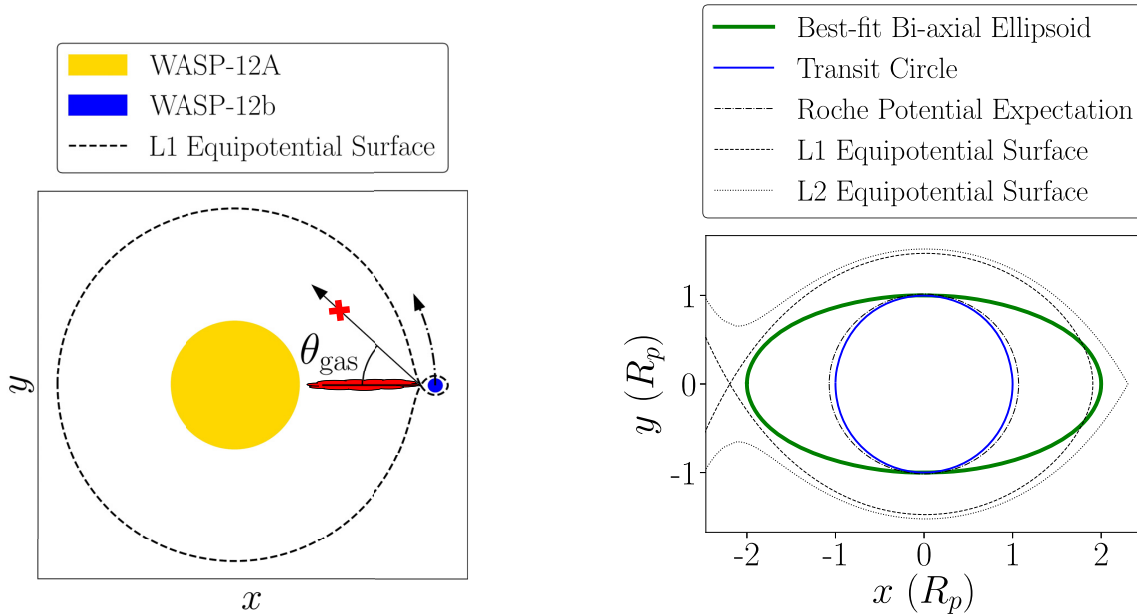


Figure 2. Bird’s-eye views of the WASP-12 system to scale. Left: while the planet is appreciably filling its Roche lobe and is expected to be tidally distorted, the star should not. Overplotted is a depiction of the direction that gas would flow after passing through the L1 Lagrange point (θ_{gas}) previously predicted to be 53.4° (Lai, Helling & van den Heuvel 2010). If our observations probe the gas stream, we can firmly reject this ballistic trajectory hypothesis as the gas appears to be aligned along the star–planet axis (indicated by the red elongated patch of gas). The direction of the planet’s orbit is shown with a dashed–dotted arrow. Right: best-fitting bi-axial ellipsoid model fit to the 2013 phase curve observation at $4.5 \mu\text{m}$, placed in the context of the planet’s Roche lobe. This shape varies drastically from that of a Roche lobe and instead suggests that our observations are probing something other than the planet’s tidally distorted shape. Also shown is a circle with the area seen at transit, the equipotential surface which would give that transit area, and the L1 and L2 equipotential surfaces. The x - and y -axes lie within the orbital plane; during transit the x -axis is parallel to our line of sight.

transit depth and may remain consistent with the smaller apparent radius at $4.5 \mu\text{m}$ compared to $3.6 \mu\text{m}$. Radiative transfer simulations based on the ‘FvrB’ mass-loss model (Matsakos et al. 2015) would allow for this hypothesis to be tested.

4.3 Radiation mechanisms

4.3.1 Blackbody emission

The discrepant second-order sinusoidal amplitudes at 3.6 and $4.5 \mu\text{m}$ can be explained by one of two emission mechanisms. First, blackbody emission could allow for greater flux at $4.5 \mu\text{m}$ than at $3.6 \mu\text{m}$ if the gas is sufficiently cool that the $3.6 \mu\text{m}$ bandpass lies on the Wien side of the blackbody curve; this scenario would allow us to place an upper limit on the temperature and spatial extent of the emitting gas, which we pursue below.

Using the host star’s effective temperature of $6300 \pm 150 \text{ K}$ (Hebb et al. 2009), we assume the host star emits as a blackbody and convert the second-order sinusoidal curves from units of F_{day}/F_* to B_λ as shown in the middle panel of Fig. 3. We adopt the fiducial $4.5 \mu\text{m}$ parameters from 2010, but set the second-order phase offset to 90° , since there is no evidence for an appreciable offset from the star–planet axis. We then take the best fit and the 1σ and 2σ upper limits on the amplitude of the $3.6 \mu\text{m}$ second-order sinusoidal variations from M. Zhang’s analysis using the second-order astrophysical model. We assume that none of the flux seen during planetary transit/eclipse is from emission by the gas. By assuming the emitting area is the same at 3.6 and $4.5 \mu\text{m}$, we can use the relative amounts of flux at these two wavelengths to determine the blackbody temperature of the gas.

Given the assumption that our observations are explained by blackbody emission, we can then place a 2σ upper limit of 619 K on the gas temperature. For reference, a temperature of 816 K would provide equal flux in both bandpasses. Attributing any of the ‘nightside’ flux to emission from the gas only lowers this limit further. Also, as WASP-12b’s skin temperature (Goody & Walker 1972) is $0.5^{0.25} T_{\text{b,day}} \approx 2500 \text{ K}$, this gas cannot be the upper layers of the planet’s atmosphere.

By taking the ratio between the flux emitted by the gas and that emitted by the star, we can determine the effective emitting area required to produce the phase curve observations. As shown in the bottom panel of Fig. 3, less emission at $3.6 \mu\text{m}$ requires lower temperature gas and therefore a larger emitting area. We can therefore place a 2σ lower-limit on the effective emitting area of the gas of 0.98 times the planet’s transiting area when seen at planetary quadrature, given the assumption that our observations are explained by blackbody emission. Attributing any of the nightside flux to emission from the gas slightly increases this limit and allows for a non-zero emitting area during planetary transit and eclipse.

4.3.2 CO emission

An alternative explanation for the increased flux at $4.5 \mu\text{m}$ is emission by CO which has its strong $\Delta V = 1$ band around $4.5 \mu\text{m}$ (see Fig. A1 in Appendix A for the CO line intensities); CO emission has previously been predicted for gas lost from WASP-12b (Li et al. 2010; Deming et al. 2011). The CO molecule should be dissociated in the planetary upper atmosphere due to the strong UV and X-ray flux from the host star which also drives most of the observed atmospheric escape seen at NUV wavelengths (Fossati et al. 2010;

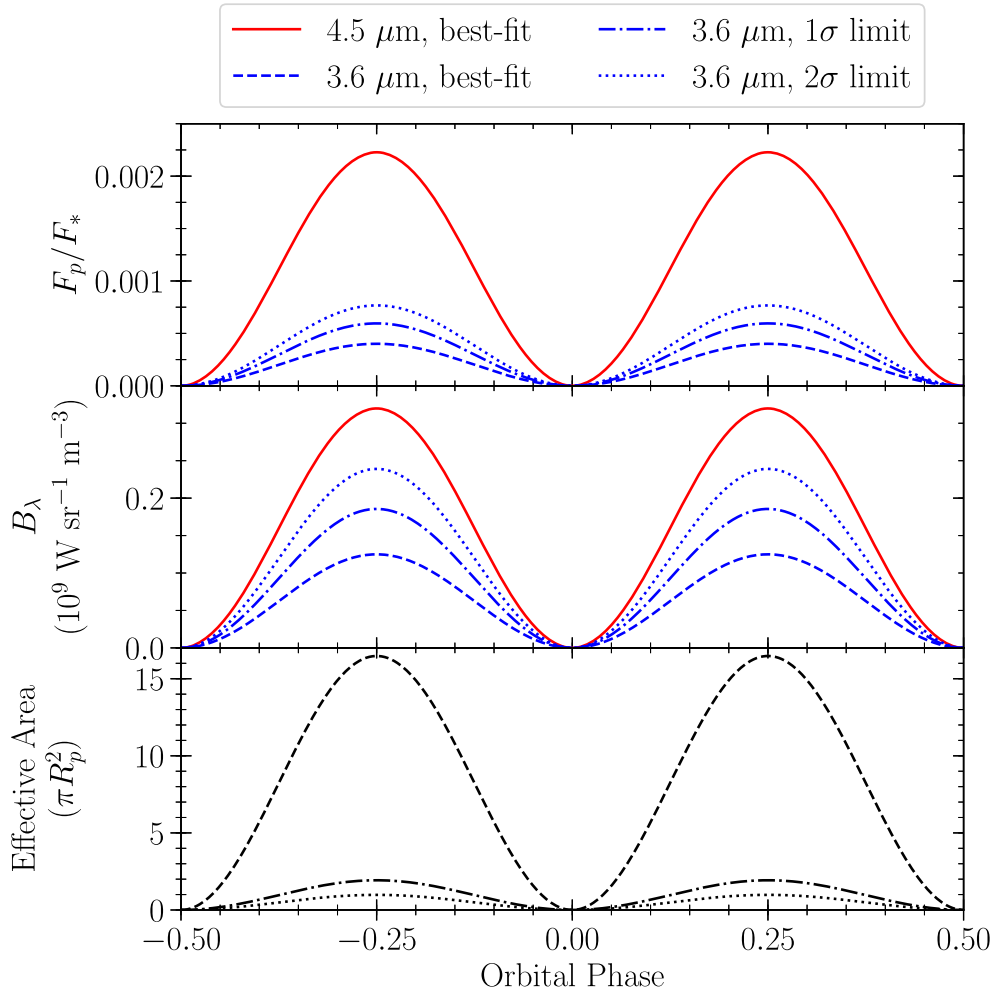


Figure 3. Limits on the emitting area required to explain the strong detection of second-order sinusoidal variations at 4.5 μm but not at 3.6 μm . Top: the emitting-body to star flux ratio for the second-order sinusoidal component of the 4.5 and 3.6 μm data (temporarily assuming a constant radius of R_p). Middle: the emitting-body’s blackbody flux assuming both wavelengths probe the same area. Bottom: the effective emitting area of the emitting blackbody required to explain the observations. The inferred gas temperatures for the 0σ , 1σ , and 2σ limits are 420, 549, and 619 K, respectively.

Haswell et al. 2012; Nichols et al. 2015); the dissociation energy of CO corresponds to a wavelength of roughly 110 nm. However, the atomic carbon and oxygen from the upper layers of the planet’s atmosphere could recombine in a gas stream where the density gets higher because of stellar wind confinement and the ‘shadow effect’ from the material in the stream closer to the star. Given a gas temperature profile (Salz et al. 2016) and our calculations of the thermal dissociation fraction of CO using the Saha equation (Bell & Cowan 2018), we find that any CO emission must either be produced within $\sim 0.1 R_p$ of the planet’s surface or beyond $2.5 R_p$. In the case of a bow shock supported by mass loss from the planet, gas temperatures are predicted to reach 10^3 – 10^4 K (Turner et al. 2016) which should allow for stable CO, provided there is sufficient UV shielding from gas nearer to the star. Simulations of the behaviour of CO in these environments are required to determine the feasibility of this molecule recombining once in a stream and emitting sufficiently strongly to explain our observations.

4.4 A note on eclipse depths

It is important to note that our reported ‘eclipse depths’ (F_{day}/F_*) are measured with respect to the phase curve value expected at

the centre of eclipse and are not measured with respect to pre-ingress and post-egress flux measurements as would be the case for observations of only the eclipse. Given our fitted phase curve parameters for WASP-12b, the difference between our reported value and using the average of pre-ingress and post-egress baselines is ~ 9 percent of F_{day}/F_* at both *Spitzer* bandpasses (assuming these baseline durations are both the same duration as the eclipse duration). This bias in eclipse observations occurs because the phase variations before ingress and after egress are flattened out by most decorrelation routines when solely observing the eclipse. For most exoplanets whose phase variations will be concave down around eclipse (like WASP-12b when seen at 3.6 μm), eclipse observations will underestimate F_{day}/F_* . For the unusual case of WASP-12b’s 4.5 μm phase variations which are concave up near eclipse, eclipse observations will overestimate F_{day}/F_* . This effect is particularly important for short-period planets which undergo significant rotation throughout the duration of eclipse observations and whose strong day–night temperature contrast cause strong phase variations over this time span. Among other things, this may explain the discrepancies between reported 3.6 and 4.5 μm eclipse depths from full-orbit phase curves (Cowan et al. 2012) and eclipse-only observations (Madhusudhan et al. 2011; Stevenson et al. 2014b), and

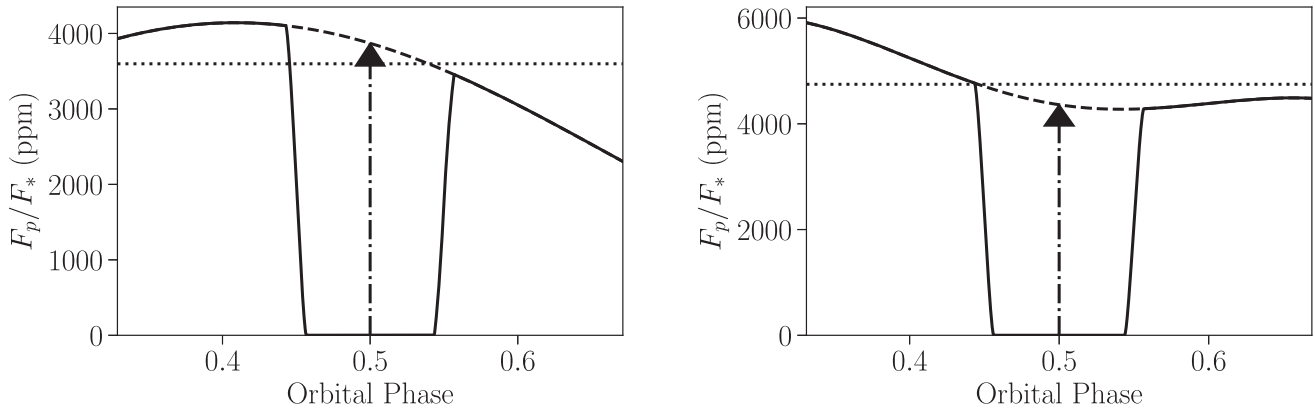


Figure 4. Bias present in eclipse-only observations of exoplanets. Left: our fiducial model for the 2010 phase curve at $3.6\ \mu\text{m}$ is shown with a solid line, while the model neglecting the secondary eclipse is shown with a dashed line. It is with respect to this line that we calculate our eclipse depth (shown with a dashed–dotted arrow), while the eclipse depth that would be measured using eclipse-only observations is shown with a dotted line. This bias occurs because there is insufficient evidence of phase variations with eclipse-only observations, so a flat or a sloped line is used instead. Right: the same bias at $4.5\ \mu\text{m}$, but in the opposite direction due to the abnormal concave-up phase variations near the $4.5\ \mu\text{m}$ eclipse.

the associated inference of C/O ratio. See Fig. 4 for a demonstration of this effect.

5 DISCUSSION AND CONCLUSIONS

By independently analysing and then combining two sets of 3.6 and $4.5\ \mu\text{m}$ *Spitzer* phase curves of the UHJ WASP-12b, we have conclusively detected strong and persistent second-order sinusoidal variations at $4.5\ \mu\text{m}$ and placed stringent upper limits on these variations at $3.6\ \mu\text{m}$. These observations of WASP-12b raise several questions which will require further study to resolve.

Our two emission hypotheses could be distinguished with phase curve observations of the ~ 1.6 and/or $2.29\ \mu\text{m}$ CO emission bands and/or with phase curve observations at wavelengths longer than $5\ \mu\text{m}$ which should exhibit strong second-order sinusoidal variations if the 3.6 versus $4.5\ \mu\text{m}$ amplitude discrepancy is the result of blackbody emission. The high precision and wavelength coverage achievable with the *James Webb Space Telescope* should allow these two emission hypotheses to be tested. The $\sim 1.6\ \mu\text{m}$ CO emission band also lies within the *Hubble* Wide Field Camera 3 bandpass and may be detectable with phase curve observations.

Critically, future models must also address the fact that the fitted planetary radius is significantly smaller at $4.5\ \mu\text{m}$ than at $3.6\ \mu\text{m}$; this may be the result of unocculted emitting gas. Combined hydrodynamic and radiative transfer simulations are required to fully understand this system. These simulations will allow us to determine the location and spatial extent of the emitting gas, and they may resolve the apparent tension between the constraint from these observations that the gas is well aligned with the star–planet axis, while NUV observations which probe lower density gas show that the gas flows significantly ahead of the planet. Understanding the nature of the increased emission at $4.5\ \mu\text{m}$ will also require modelling the mass loss and the UV dissociation and potential recombination of CO molecules as they flow from the planet’s upper atmosphere through a gas stream and potentially experience a shock. These models may also assist in understanding the observed hotspot variability seen at $3.6\ \mu\text{m}$.

Finally, while WASP-12b is one of the exoplanets closest to overflowing its Roche lobe (see Fig. A2), there are several other UHJs with similar characteristics with published *Spitzer* phase curves that do not show strong second-order sinusoidal variations

at $4.5\ \mu\text{m}$: particularly WASP-19b (Wong et al. 2016), WASP-33b (Zhang et al. 2018), and WASP-103b (Kreidberg et al. 2018). One potential explanation is that WASP-12b’s orbit may be decaying (Maciejewski et al. 2016; Patra et al. 2017), while the other exoplanets may be more stable; this could potentially be explained if WASP-12b was locked in a high obliquity state due to a resonance with a perturbing planet which could drive orbital decay and inflate the planet beyond its Roche lobe (Millholland & Laughlin 2018). Alternatively, the high-energy irradiation from WASP-12A may be stronger than the other UHJ host stars. Further research is required to understand why WASP-12b is the only exoplanet known to be exhibiting these exceptionally strong second-order sinusoidal variations at $4.5\ \mu\text{m}$.

ACKNOWLEDGEMENTS

TJB acknowledges support from the McGill Space Institute Graduate Fellowship, the Natural Sciences and Engineering Research Council of Canada’s Postgraduate Scholarships-Doctoral Fellowship, and from the Fonds de recherche du Québec – Nature et technologies through the Centre de Recherche en Astrophysique du Québec. The research leading to these results has received funding from the European Research Council (ERC) under the European Union’s Horizon 2020 research and innovation programme (grant agreement no. 679633; Exo-Atmos). TJB, LD, and NBC are also affiliated with, and supported by, the McGill Space Institute, the Institute for Research on Exoplanets, and the Centre for Research in Astrophysics of Quebec. We have also made use of open-source software provided by the PYTHON, ASTROPY, SCIPY, and MATPLOTLIB communities.

REFERENCES

- Arcangeli J. et al., 2018, *ApJ*, 855, L30
- Armstrong D. J., de Mooij E., Barstow J., Osborn H. P., Blake J., Saniee N. F., 2016, *Nat. Astron.*, 1, 0004
- Artigau É., Bouchard S., Doyon R., Lafrenière D., 2009, *ApJ*, 701, 1534
- Bailey A., Goodman J., 2019, *MNRAS*, 482, 1872
- Bechter E. B. et al., 2014, *ApJ*, 788, 2
- Bell T. J., Cowan N. B., 2018, *ApJ*, 857, L20
- Bell T. J. et al., 2017, *ApJ*, 847, L2

- Bergfors C., Brandner W., Henning T., Daemgen S., 2011, in Sozzetti A., Lattanzi M. G., Boss A. P., eds, IAU Symp. Vol. 276, *The Astrophysics of Planetary Systems: Formation, Structure, and Dynamical Evolution*. Kluwer, Dordrecht, p. 397
- Bisikalo D., Kaygorodov P., Ionov D., Shematovich V., Lammer H., Fossati L., 2013b, *ApJ*, 764, 19
- Bisikalo D. V., Kaigorodov P. V., Ionov D. E., Shematovich V. I., 2013a, *Astron. Rep.*, 57, 715
- Budaj J., 2011, *AJ*, 141, 59
- Burrows A., Hubeny I., Budaj J., Knutson H. A., Charbonneau D., 2007, *ApJ*, 668, L171
- Burrows A., Budaj J., Hubeny I., 2008, *ApJ*, 678, 1436
- Burton J. R., Watson C. A., Fitzsimmons A., Pollacco D., Moulds V., Littlefair S. P., Wheatley P. J., 2014, *ApJ*, 789, 113
- Campo C. J. et al., 2011, *ApJ*, 727, 125
- Charbonneau D., Knutson H. A., Barman T., Allen L. E., Mayor M., Megeath S. T., Queloz D., Udry S., 2008, *ApJ*, 686, 1341
- Cherenkov A. A., Bisikalo D. V., Kaigorodov P. V., 2014, *Astron. Rep.*, 58, 679
- Collins K. A., Kielkopf J. F., Stassun K. G., 2017, *AJ*, 153, 78
- Cowan N. B., Agol E., 2011, *ApJ*, 729, 54
- Cowan N. B., Agol E., Charbonneau D., 2007, *MNRAS*, 379, 641
- Cowan N. B., Machalek P., Croll B., Shekhtman L. M., Burrows A., Deming D., Greene T., Hora J. L., 2012, *ApJ*, 747, 82
- Cowan N. B., Fuentes P. A., Haggard H. M., 2013, *MNRAS*, 434, 2465
- Croll B., Lafreniere D., Albert L., Jayawardhana R., Fortney J. J., Murray N., 2011, *AJ*, 141, 30
- Crossfield I. J. M., Hansen B. M. S., Harrington J., Cho J. Y.-K., Deming D., Menou K., Seager S., 2010, *ApJ*, 723, 1436
- Crossfield I. J. M., Knutson H., Fortney J., Showman A. P., Cowan N. B., Deming D., 2012a, *ApJ*, 752, 81
- Crossfield I. J. M., Barman T., Hansen B. M. S., Tanaka I., Kodama T., 2012b, *ApJ*, 760, 140
- Cubillos P. et al., 2013, *ApJ*, 768, 42
- Cubillos P., Harrington J., Madhusudhan N., Foster A. S. D., Lust N. B., Hardy R. A., Bowman M. O., 2014, *ApJ*, 797, 42
- Cubillos P., Harrington J., Loredo T. J., Lust N. B., Bleicic J., Stemm M., 2017, *AJ*, 153, 3
- Dang L. et al., 2018, *Nat. Astron.*, 2, 220
- de Wit J., Lewis N. K., Langton J., Laughlin G., Deming D., Batygin K., Fortney J. J., 2016, *ApJ*, 820, L33
- de Wit J. et al., 2017, *ApJ*, 836, L17
- Debrecht A., Carroll-Nellenback J., Frank A., Fossati L., Blackman E. G., Dobbs-Dixon I., 2018, *MNRAS*, 478, 2592
- Deming D. et al., 2011, *ApJ*, 726, 95
- Demory B.-O., Gillon M., Madhusudhan N., Queloz D., 2016, *MNRAS*, 455, 2018
- Espinosa Lara F., Rieutord M., 2011, *A&A*, 533, A43
- Foreman-Mackey D., Hogg D. W., Lang D., Goodman J., 2013, *PASP*, 125, 306
- Fossati L. et al., 2010, *ApJ*, 714, L222
- Fossati L., Ayres T. R., Haswell C. A., Bohlender D., Kochukhov O., Flöer L., 2013, *ApJ*, 766, L20
- Gelman A., Rubin D. B., 1992, *Stat. Sci.*, 7, 457
- Goody R. M., Walker J. C. G., 1972, *Atmospheres, Foundations of Earth Science Series*. Prentice-Hall, Upper Saddle River, NJ
- Harrington J., Hansen B. M., Luszcz S. H., Seager S., Deming D., Menou K., Cho J. Y.-K., Richardson L. J., 2006, *Science*, 314, 623
- Haswell C. A. et al., 2012, *ApJ*, 760, 79
- Hebb L. et al., 2009, *ApJ*, 693, 1920
- Husser T.-O., Wende-von Berg S., Dreizler S., Homeier D., Reiners A., Barman T., Hauschildt P. H., 2013, *A&A*, 553, A6
- Ingalls J. G. et al., 2016, *AJ*, 152, 44
- Kipping D. M., 2013, *MNRAS*, 435, 2152
- Knutson H. A. et al., 2007, *Nature*, 447, 183
- Knutson H. A. et al., 2009a, *ApJ*, 690, 822
- Knutson H. A., Charbonneau D., Cowan N. B., Fortney J. J., Showman A. P., Agol E., Henry G. W., 2009b, *ApJ*, 703, 769
- Knutson H. A., Howard A. W., Isaacson H., 2010, *ApJ*, 720, 1569
- Knutson H. A. et al., 2012, *ApJ*, 754, 22
- Komacek T. D., Tan X., 2018, *Res. Notes Am. Astron. Soc.*, 2, 36
- Kreidberg L., 2015, *PASP*, 127, 1161
- Kreidberg L. et al., 2018, *AJ*, 156, 17
- Krick J. E. et al., 2016, *ApJ*, 824, 27
- Lai D., Helling C., van den Heuvel E. P. J., 2010, *ApJ*, 721, 923
- Laughlin G., Deming D., Langton J., Kasen D., Vogt S., Butler P., Rivera E., Meschiari S., 2009, *Nature*, 457, 562
- Leconte J., Lai D., Chabrier G., 2011a, *A&A*, 528, A41
- Leconte J., Lai D., Chabrier G., 2011b, *A&A*, 536, C1
- Lewis N. K. et al., 2013, *ApJ*, 766, 95
- Li S.-L., Miller N., Lin D. N. C., Fortney J. J., 2010, *Nature*, 463, 1054
- Llama J., Wood K., Jardine M., Vidotto A. A., Helling C., Fossati L., Haswell C. A., 2011, *MNRAS*, 416, L41
- Llama J., Vidotto A. A., Jardine M., Wood K., Fares R., Gombosi T. I., 2013, *MNRAS*, 436, 2179
- Lothringer J. D., Barman T., Koskinen T., 2018, *ApJ*, 866, 27
- Lust N. B., Britt D., Harrington J., Nymeyer S., Stevenson K. B., Ross E. L., Bowman W., Fraine J., 2014, *PASP*, 126, 1092
- Maciejewski G. et al., 2016, *A&A*, 588, L6
- Madhusudhan N. et al., 2011, *Nature*, 469, 64
- Mandel K., Agol E., 2002, *ApJ*, 580, L171
- Mansfield M. et al., 2018, *AJ*, 156, 10
- Matsakos T., Uribe A., Königl A., 2015, *A&A*, 578, A6
- Maxted P. F. L. et al., 2013, *MNRAS*, 428, 2645
- Millholland S., Laughlin G., 2018, *ApJ*, 869, L15
- Nichols J. D. et al., 2015, *ApJ*, 803, 9
- Nymeyer S. et al., 2011, *ApJ*, 742, 35
- Parmentier V. et al., 2018, *A&A*, 617, A110
- Patra K. C., Winn J. N., Holman M. J., Yu L., Deming D., Dai F., 2017, *AJ*, 154, 4
- Radigan J., Jayawardhana R., Lafrenière D., Artigau É., Marley M., Saumon D., 2012, *ApJ*, 750, 105
- Roche E., 1847, *Mém. Sect. Sci.*, 1, 243
- Rogers T. M., 2017, *Nat. Astron.*, 1, 0131
- Rothman L. S. et al., 2010, *J. Quant. Spectrosc. Radiat. Transf.*, 111, 2139
- Salz M., Czesla S., Schneider P. C., Schmitt J. H. M. M., 2016, *A&A*, 586, A75
- Schwartz J. C., Cowan N. B., 2017, *PASP*, 129, 014001
- Shporer A. et al., 2019, *AJ*, 157, 178
- Sing D. K., 2010, *A&A*, 510, A21
- Skidmore W., Welsh W. F., Wood J. H., Stiening R. F., 1997, *MNRAS*, 288, 189
- Stevenson K. et al., 2010, *Nature*, 464, 1161
- Stevenson K. B. et al., 2012a, *ApJ*, 754, 136
- Stevenson K. B. et al., 2012b, *ApJ*, 755, 9
- Stevenson K. B., Bean J. L., Seifahrt A., Désert J.-M., Madhusudhan N., Bergmann M., Kreidberg L., Homeier D., 2014a, *AJ*, 147, 161
- Stevenson K. B., Bean J. L., Madhusudhan N., Harrington J., 2014b, *ApJ*, 791, 36
- Stevenson K. B. et al., 2017, *AJ*, 153, 68
- ter Braak C. J. F., Vrugt J. A., 2008, *Stat. Comput.*, 18, 435
- Turner J. D., Christie D., Arras P., Johnson R. E., Schmidt C., 2016, *MNRAS*, 458, 3880
- Vidotto A. A., Jardine M., Helling C., 2010, *ApJ*, 722, L168
- Vidotto A. A., Jardine M., Helling C., 2011, *MNRAS*, 414, 1573
- Welsh W. F., Orosz J. A., Seager S., Fortney J. J., Jenkins J., Rowe J. F., Koch D., Borucki W. J., 2010, *ApJ*, 713, L145
- Winn J. N. et al., 2007, *AJ*, 134, 1707
- Wong I. et al., 2015, *ApJ*, 811, 122
- Wong I. et al., 2016, *ApJ*, 823, 122
- Zellem R. T. et al., 2014, *ApJ*, 790, 53
- Zellem R. T. et al., 2017, *ApJ*, 844, 27
- Zhang M. et al., 2018, *AJ*, 155, 83

SUPPORTING INFORMATION

Supplementary data are available at [MNRAS](#) online.

Figure 1. Same as Fig. A5, but for the 2010 (left) and 2013 (right) 3.6 μm observations of WASP-12b, fit using the SPCA Poly4 (2010) and SPCA Poly3* $f(t)$ (2013) detector models and the second- (2010) and first-order (2013) phase variations model.

Figure 2. Same figure as Fig. A5, but for the 2010 (left) and 2013 (right) 4.5 μm observations of WASP-12b, both fit using the SPCA BLISS detector model and the second-order phase variations model.

Figure 3. Same figure as Fig. A5, but for the 2010 (left) and 2013 (right) 3.6 μm observations of WASP-12b, both fit using the POET pipeline.

Figure 4. Same figure as Fig. A5 but for the 2010 (left) and 2013 (right) 4.5 μm observations of WASP-12b, both fit using the POET pipeline.

Table A3. Best-fitting 3.6 μm phase curve parameters from 2010.

Table A4. Best-fitting 3.6 μm phase curve parameters from 2013.

Table A5. Best-fitting 3.6 μm planetary parameters from 2010.

Table A6. Best-fitting 3.6 μm planetary parameters from 2013.

Table A7. Best-fitting 4.5 μm phase curve parameters from 2010.

Table A8. Best-fitting 4.5 μm phase curve parameters from 2013.

Table A9. Best-fitting 4.5 μm planetary parameters from 2010.

Table A10. Best-fitting 4.5 μm planetary parameters from 2013.

Please note: Oxford University Press is not responsible for the content or functionality of any supporting materials supplied by the authors. Any queries (other than missing material) should be directed to the corresponding author for the article.

APPENDIX A: CORRECTION FOR DILUTION BY STELLAR COMPANIONS

To correct for the dilution of our light curves by the nearby stellar companions WASP-12BC, we apply the dilution factors from Stevenson et al. (2014a): $\alpha_{\text{comp}} = 0.1149 \pm 0.0039$ and 0.1196 ± 0.0042 for 3.6 and 4.5 μm , respectively. Since our phase curve amplitudes are normalized by the eclipse depth, no corrections need to be made to C_1 , D_1 , C_2 , or D_2 . Additionally, while the planetary radii need to be corrected for dilution from WASP-12BC,

the ratio $R_{p,2}/R_p$ remains the same for models with ellipsoidal variations. Following Stevenson et al. (2014a,b), the multiplicative correction factor is

$$C_{\text{corr}}(\lambda) = 1 + g(\beta, \lambda)\alpha_{\text{comp}}(\lambda),$$

where $g(\beta, \lambda)$ is the fraction of WASP-12BC's flux which falls within our aperture of size β . We estimated $g(\beta, \lambda)$ using STINYTIM,² the point response function modelling software for *Spitzer*. We made 10 times oversampled point response functions calculated at the pixel position (25,25) assuming a $T = 3660$ blackbody source (the effective temperature of WASP-12BC; Stevenson et al. 2014b). We found $g(2.5, 4.5 \mu\text{m}) = 0.8147$, $g(3.2, 4.5 \mu\text{m}) = 0.8608$, $g(4.3, 3.6 \mu\text{m}) = 0.9089$, and $g(2.9, 3.6 \mu\text{m}) = 0.8580$. For the 3×3 pixel stamp used in M. Zhang's PLD analyses, we find $g(3 \times 3, 3.6 \mu\text{m}) = 0.6518$ and $g(3 \times 3, 4.5 \mu\text{m}) = 0.6291$. For P. Cubillos' analyses, we find $g(3.0, 4.5 \mu\text{m}) = 0.8533$, $g(2.5, 4.5 \mu\text{m}) = 0.6957$, $g(2.5, 3.6 \mu\text{m}) = 0.8254$, and $g(4.0, 3.6 \mu\text{m}) = 0.9015$. We also checked $g(2.25, 3.6 \mu\text{m})$ and $g(2.25, 4.5 \mu\text{m})$ to compare our calculation to that of Stevenson et al. (2014b); we find values of 0.8007 and 0.7586, where Stevenson et al. (2014b) found 0.7116 and 0.6931. This discrepancy is likely caused by an incorrect angular separation used in the previous work's calculation.

The planet's radius was then corrected using

$$R_{p,\text{corr}}(\lambda) = \sqrt{C_{\text{corr}}(\lambda)} R_{p,\text{meas}}(\lambda),$$

with the elongated axis, $R_{p,2}$, in bi-axial ellipsoid models corrected similarly. The day-side flux was corrected using

$$F_{\text{day,corr}}(\lambda) = C_{\text{corr}}(\lambda) F_{\text{day,meas}}(\lambda),$$

with the white noise amplitude, σ_F , corrected similarly.

²<http://irsa.ipac.caltech.edu/data/SPITZER/docs/dataanalysis/tools/tools/contributed/general/stinytim/>

Table A1. A summary of all the priors used in the three independent analyses. Uniform priors were used where there are inequalities below, Gaussian priors were used where uncertainties are indicated, variables were fixed where only a value is indicated, and parameters were unconstrained where Free is written.

	Zhang PLD	Bell SPCA	Cubillos POET
t_0 (BMJD)	$54508.20396 < t_0 < 54508.74968$	$56176.16825800 \pm 0.00007765$	Free
R_p/R_*	>0	$0 < R_p/R_* < 1$	>0
a/R_*	3.039	3.039 ± 0.034	3.039 ± 0.034
i (deg)	83.37	83.37 ± 0.68	83.37 ± 0.68 (fitted cos i)
P (d)	1.09142245	1.0914203	1.0914203
F_p/F_*	Free	$0 < F_p/F_* < 1$	>0
C_1	Free	Positive phase curve	Positive phase curve
D_1	Free	Positive phase curve	Positive phase curve
C_2	Free	Positive phase curve	Positive phase curve
D_2	Free	Positive phase curve	Positive phase curve
$R_{p,2}/R_*$	>0	$0 < R_{p,2} < 1$	>0
σ_F/F_* (white noise)	$0 < \sigma_F/F_* < 1$	>0	Free
Limb darkening	Sing (2010) model	$0 < q_1 < 1$; $0 < q_2 < 1$	$0 < q_1 < 1$; $0 < q_2 < 1$
e	0	0	t_{eclipse} : Free; $t_{14,\text{eclipse}} > 0$; $t_{12,\text{eclipse}} > 0$; $t_{34} = t_{12}$
Instrumental variables	Free (PLD coefficients, slope in time)	Free (polynomial coefficients, slope in time for 2013 3.6 μm)	Free (slope in time for 2013 4.5 μm)

Table A2. 3.6 and 4.5 μm phase curve parameters from the preferred models for 2010 and 2013. Fiducial models are indicated with bolding.

3.6 μm

Data Set	Model	C_1	D_1	C_2	D_2	F_{day}/F_* ‡ (ppm)	$\frac{\ln(L)}{N_{\text{data}}}$ †
2010	Bell Poly4, 2nd Order	0.436 ± 0.033	-0.067 ± 0.061	0.027 ± 0.028	0.076 ± 0.022	3840 ± 210	5.2
2010	Zhang PLD, 1st Order	0.371 ± 0.051	-0.239 ± 0.046			3870 ± 130	5.62
2010	Cubillos BLISS, 1st Order	0.395 ± 0.036	-0.237 ± 0.036			3780 ± 120	3.65
2013	Bell Poly3*f(t), 1st Order	0.299 ± 0.029	0.105 ± 0.030			3970 ± 150	5.37
2013	Zhang PLD, 1st Order	0.320 ± 0.024	0.079 ± 0.025			3840 ± 120	5.6
2013	Cubillos BLISS, 1st Order	0.324 ± 0.024	0.091 ± 0.023			3810 ± 120	3.59

3.6 μm , cont.

Data Set	Model	R_p/R_* ‡	Phase Offset (degrees)		$T_{b,\text{day}}$ † (K)	$T_{b,\text{night}}$ † (K)	$\frac{\ln(L)}{N_{\text{data}}}$ †
			1st Order†	2nd Order†			
2010	Bell Poly4, 2nd Order	0.1197 ± 0.0012	-8.8 ± 7.9	144.7 ± 9.6	2655 ± 76	1190 ± 180	5.2
2010	Zhang PLD, 1st Order	0.11642 ± 0.00063	-32.6 ± 6.2		2744 ± 48	1510 ± 210	5.62
2010	Cubillos BLISS, 1st Order	0.11782 ± 0.00096	-30.9 ± 4.5		2603 ± 49	1360 ± 160	3.65
2013	Bell Poly3*f(t), 1st Order	0.1159 ± 0.0011	19.3 ± 4.3		2795 ± 64	1830 ± 110	5.37
2013	Zhang PLD, 1st Order	0.11327 ± 0.00068	13.6 ± 3.8		2813 ± 48	1760 ± 97	5.60
2013	Cubillos BLISS, 1st Order	0.1169 ± 0.0011	15.7 ± 4.0		2637 ± 47	1658 ± 83	3.59

4.5 μm

Data Set	Model	C_1	D_1	C_2	D_2	F_{day}/F_* ‡ (ppm)	$\frac{\ln(L)}{N_{\text{data}}}$ †
2010	Bell BLISS, 2nd Order	0.414 ± 0.044	-0.218 ± 0.054	-0.265 ± 0.037	0.031 ± 0.025	4200 ± 200	5.22
2010	Zhang PLD, 2nd Order	0.489 ± 0.016	-0.080 ± 0.020	-0.252 ± 0.019	0.042 ± 0.014	4360 ± 140	5.45
2010	Cubillos BLISS, 2nd Order	0.476 ± 0.030	-0.137 ± 0.030	-0.263 ± 0.027	0.043 ± 0.017	4380 ± 170	3.37
2013	Bell BLISS, 2nd Order	0.271 ± 0.053	-0.096 ± 0.046	-0.303 ± 0.043	0.122 ± 0.034	3920 ± 210	5.22
2013	Zhang PLD, 2nd Order	0.395 ± 0.036	-0.136 ± 0.025	-0.307 ± 0.023	0.034 ± 0.021	3920 ± 150	5.43
2013	Cubillos BLISS, 2nd Order	0.376 ± 0.030	-0.091 ± 0.027	-0.292 ± 0.029	0.041 ± 0.020	4120 ± 160	3.41

4.5 μm , cont.

Data Set	Model	R_p/R_* ‡	Phase Offset (degrees)		$T_{b,\text{day}}$ † (K)	$T_{b,\text{night}}$ † (K)	$\frac{\ln(L)}{N_{\text{data}}}$ †
			1st Order†	2nd Order†			
2010	Bell BLISS, 2nd Order	0.1078 ± 0.0013	-27.9 ± 6.1	93.4 ± 2.7	2879 ± 91	1250 ± 240	5.22
2010	Zhang PLD, 2nd Order	0.10656 ± 0.00085	-9.5 ± 2.3	94.7 ± 1.6	2989 ± 66	790 ± 150	5.45
2010	Cubillos BLISS, 2nd Order	0.1075 ± 0.0014	-16.0 ± 3.5	94.6 ± 1.9	2965 ± 78	940 ± 210	3.37
2013	Bell BLISS, 2nd Order	0.1092 ± 0.0016	-19 ± 11	100.9 ± 3.1	2722 ± 92	1800 ± 200	5.22
2013	Zhang PLD, 2nd Order	0.1049 ± 0.0010	-19.1 ± 3.9	93.2 ± 1.9	2854 ± 74	1340 ± 180	5.43
2013	Cubillos BLISS, 2nd Order	0.1104 ± 0.0014	-13.6 ± 4.0	94.0 ± 1.9	2768 ± 73	1400 ± 140	3.41

† These are derived quantities and are not fitted directly.

‡ These quantities have been corrected for dilution from WASP-12BC (see supplementary text).

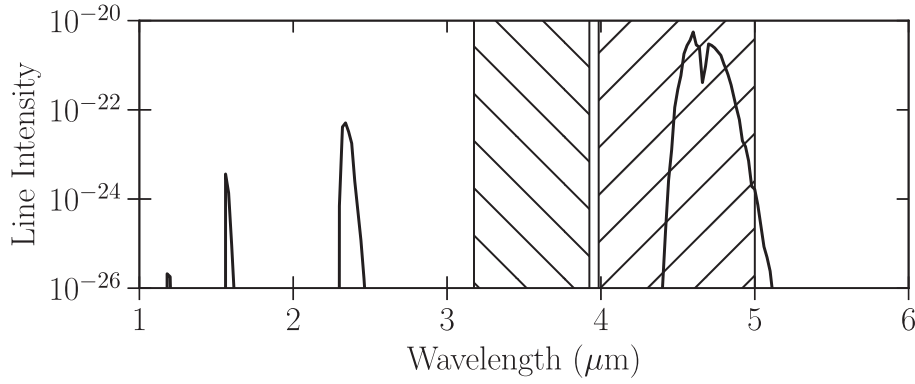


Figure A1. CO line intensities at 296 K from HITEMP (Rothman et al. 2010) in units of $\text{cm}^{-1}/(\text{molecule} \times \text{cm}^{-2})$ which has been binned to a spectral resolution of 10 cm. The bandwidths of *Spitzer*/IRAC channels 1 and 2 are respectively shown with downward sloping and upward sloping hatched regions.

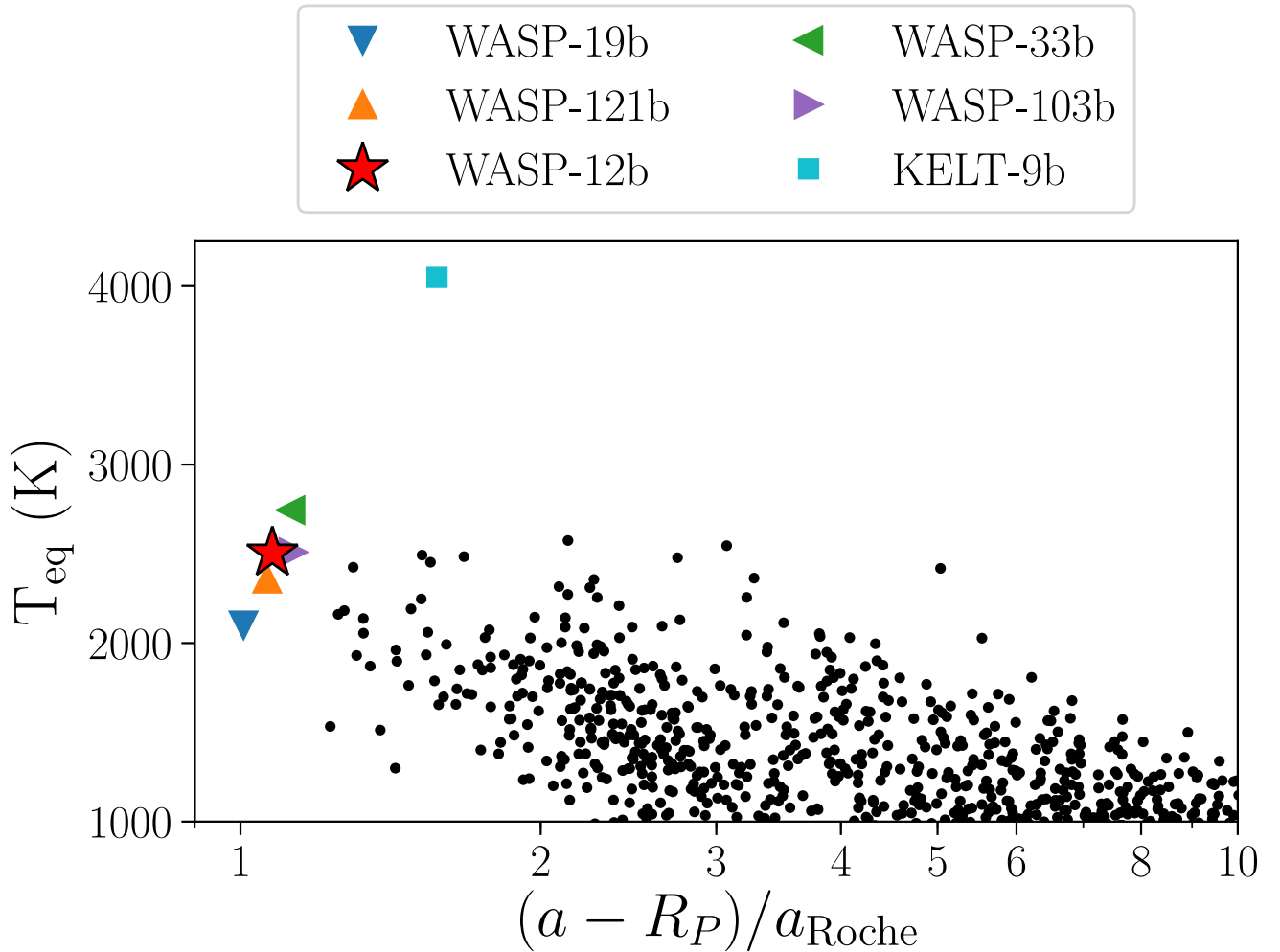


Figure A2. A comparison of WASP-12b to other exoplanets. The y-axis is the planets' equilibrium temperature ($T_{\text{eq}} = 0.25^{0.25} T_* \sqrt{R_*/a}$), and this x-axis is the distance of the substellar point on the planets from their L1 Lagrange point (Roche 1847), where $a_{\text{Roche}} = 2.44(R_p)(M_*/M_p)^{1/3}$. While WASP-12b is one of the exoplanets closest to overflowing its Roche lobe, there are several others with similar characteristics for which *Spitzer* phase curves do not show strong second-order sinusoidal variations at 4.5 μm (Wong et al. 2016; Zhang et al. 2018; Kreidberg et al. 2018). One potential explanation is that WASP-12b's orbit may be decaying (Maciejewski et al. 2016; Patra et al. 2017), while the other exoplanets may be more stable.

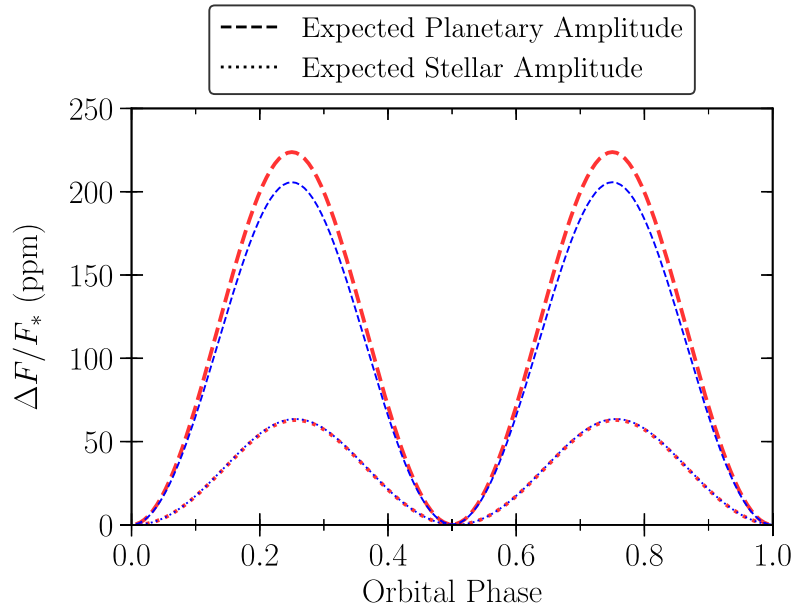


Figure A3. Expected amplitude of tidal distortion from the host star compared to that from the planet. Thin blue lines show the amplitudes at $3.6 \mu\text{m}$, while thick red lines show the amplitudes at $4.5 \mu\text{m}$.

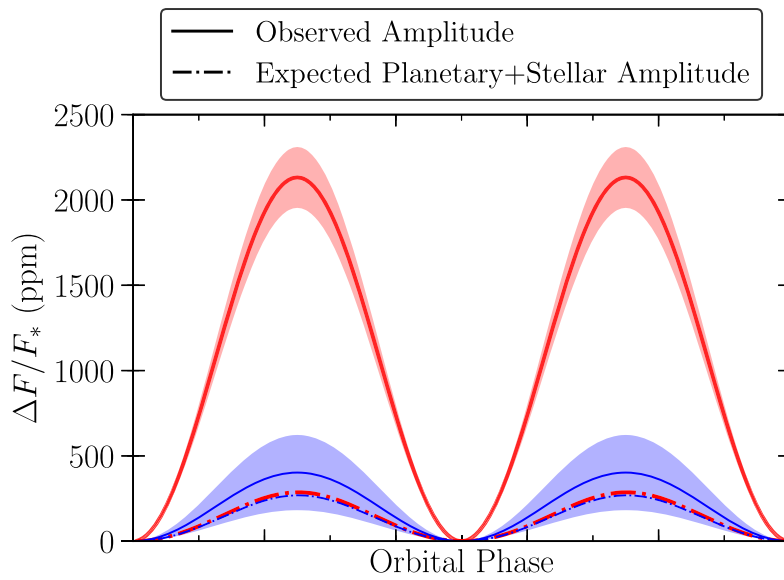


Figure A4. Observed second-order sinusoidal variations at 3.6 and $4.5 \mu\text{m}$ and their 1σ uncertainties compared to the expected amplitude of tidal distortion from the host star and the planet. The $3.6 \mu\text{m}$ phase curve is consistent with the expected amplitudes while the $4.5 \mu\text{m}$ phase curve is highly discrepant. Thin blue lines show the amplitudes at $3.6 \mu\text{m}$, while thick red lines show the amplitudes at $4.5 \mu\text{m}$.

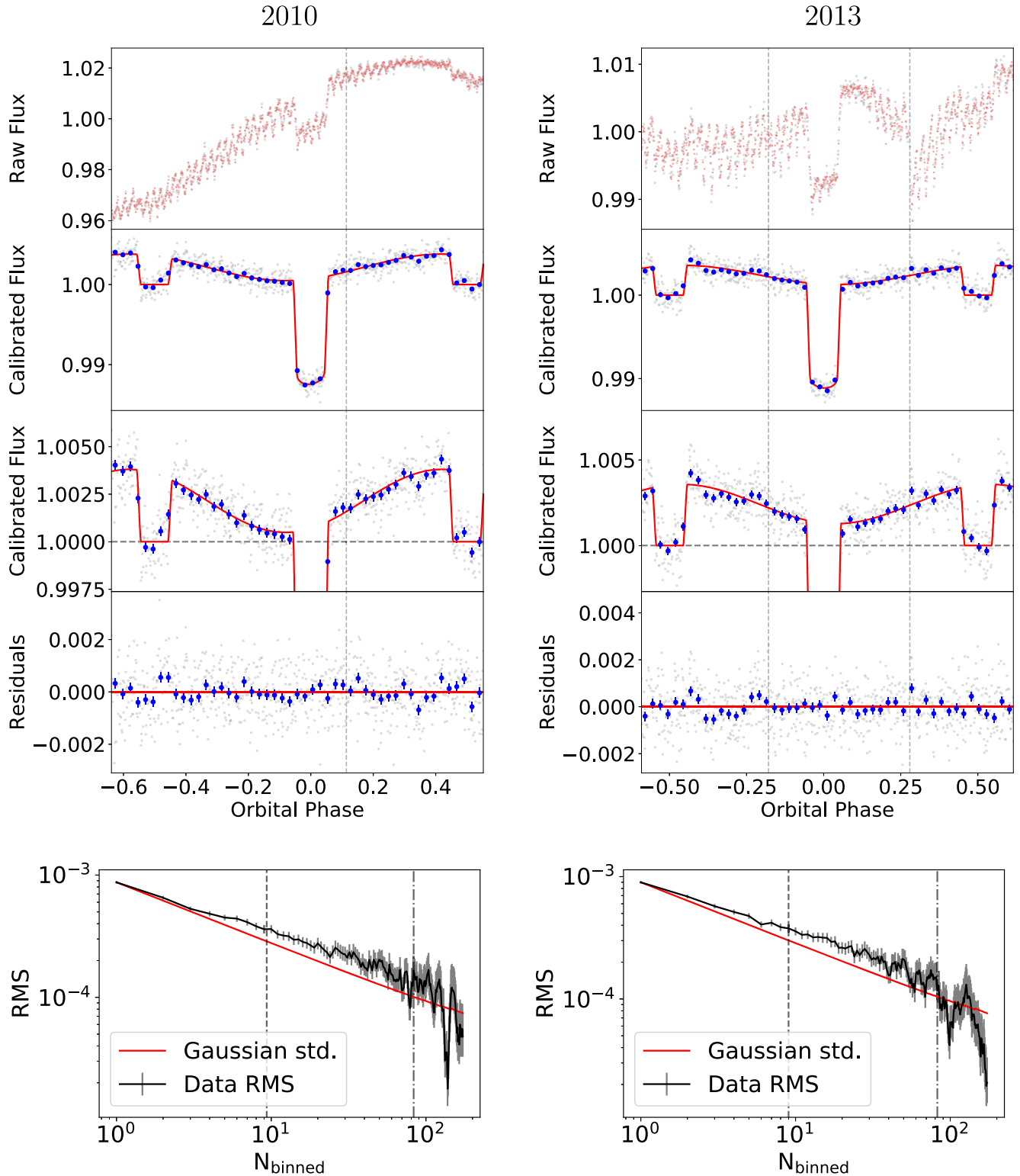


Figure A5. Top row: WASP-12b 2010 (left) and 2013 (right) $3.6 \mu\text{m}$ observations, fit using the Zhang PLD detector model and second- (2010) and first-order (2013) phase variations model. Vertical dashed lines mark the transitions between AORs. Bottom row: red noise test for the 2010 (left) and 2013 (right) $3.6 \mu\text{m}$ observations of WASP-12b for the above fits. The black line shows the decrease in the observed standard deviation in the residuals as N_{binned} (the number of data points binned together) increases. The red line shows the expected decrease in standard deviation, assuming the noise is entirely white. The close match between the two curves suggests that little-to-no red noise remains in the residuals. A vertical, dashed line shows the time-scale for transit/eclipse ingress and egress, while the dashed-dotted line shows the t_1-t_4 transit duration.

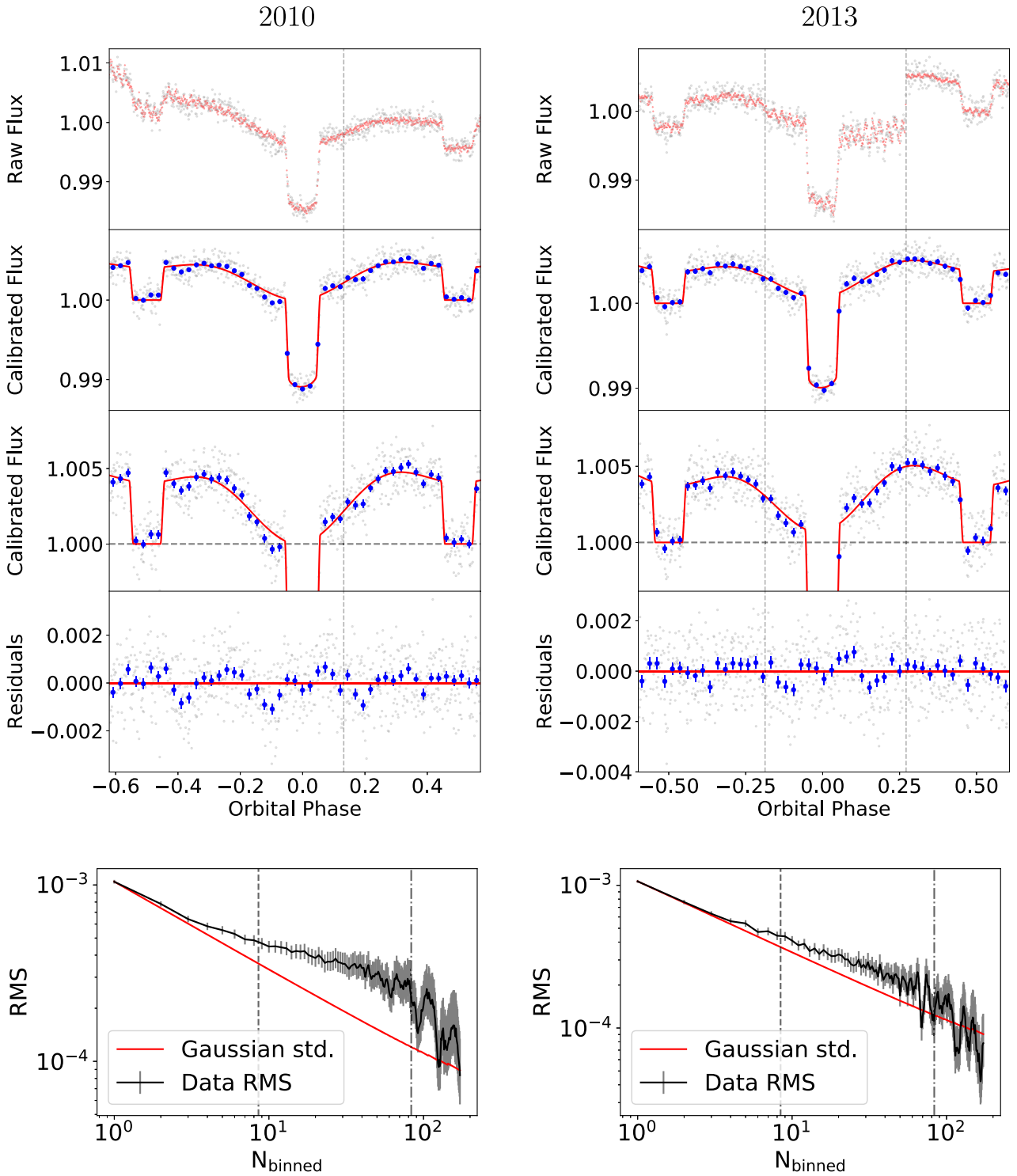


Figure A6. Same figure as the left-hand panel of Fig. A5, but for the 2010 (left-hand column) and 2013 (right-hand column) 4.5 μm observations of WASP-12b, both fit using the Zhang PLD detector model and the second-order phase variations model.

APPENDIX B: COMPUTING ASTROPHYSICAL PARAMETERS

Tables A2–A9 present many of the fitted astrophysical values from all models run in all three independent analyses. $T_{b,\text{day}}$ and $T_{b,\text{night}}$ are the apparent brightness temperatures of the planet’s day and night hemispheres which we calculate using *only the contribution from the first-order sinusoid*. In doing so, we are assuming that the second-order sinusoidal variations are attributable to something other than the planet, although the second-order sinusoidal variations end up having negligible contributions during transit and eclipse anyway. These brightness temperatures are calculated by inverting the *Planck* function (Cowan & Agol 2011), using

$$T_b(\lambda) = \frac{hc}{\lambda k_B} \left[\ln \left(1 + \frac{\exp(hc/\lambda k_B T_{*,b}) - 1}{\psi(\lambda)} \right) \right]^{-1},$$

where h is Planck’s constant, c is the speed of light, k_B is the Boltzmann constant, and λ is the wavelength. For $T_{b,\text{day}}$, $\psi = (F_{\text{day}}/F_*)(R_p/R_*)^{-2}$, and for $T_{b,\text{night}}$, $\psi = (F_{\text{day}}/F_*)(1 - 2C_1)(R_p/R_*)^{-2}$. The stellar brightness temperature, $T_{*,b}$ was calculated by fitting blackbodies to the relevant wavelengths from a PHOENIX stellar model (Husser et al. 2013) with previously measured (Hebb et al. 2009) values of $T_{*,\text{eff}} = 6300$ K and $\log(g) = 4.5$. We find $T_{*,b} = 6000$ K for $4.5 \mu\text{m}$ and 5800 K for $3.6 \mu\text{m}$. The tabulated first and second-order offsets are measured in degrees after the secondary eclipse and are calculated using:

$$\psi_1 = -(180/\pi) \arctan(D_1/C_1)$$

$$\psi_2 = 180 - 0.5(180/\pi) \arctan(D_2/C_2).$$

APPENDIX C: TIDAL DISTORTION CALCULATIONS

To assess the impact of stellar and planetary tidal distortion, we model the stellar/planetary surfaces using the dimensionless Roche potential, defined by

$$\Omega(r, \theta, \phi) = \frac{1}{r} + q \left(\frac{1}{\sqrt{1 - 2r \sin \theta \cos \phi + r^2}} - r \sin \theta \cos \phi \right) + \frac{q+1}{2} r^2 \sin^2 \theta,$$

where r is the distance from the host star, θ is the polar angle, ϕ is the azimuthal angle, and q is the mass ratio, M_*/M_p . We find that the star’s radius should be 0.0085 per cent longer along the star–planet axis compared to the perpendicular equatorial axis, while the planet’s radius should be 5.5 per cent longer along the star–planet axis compared to the dawn–dusk axis seen at transit.

We first assume that the planet and star have a constant temperature of 3000 and 6300 K, respectively, and then perturb these temperatures to account for gravity darkening using the $T_{\text{eff}} \propto g_{\text{eff}}^\beta$ model (Espinosa Lara & Rieutord 2011) where β is 0.24 for the appreciably distorted planet and 0.25 for the more spherical host star. Next, we convert these temperature maps into flux maps using the *Planck* blackbody function. We then compute disc-integrated phase curves (Cowan, Fuentes & Haggard 2013), while also accounting for the variations in apparent areas of the two objects. Our calculations show that the planet’s expected variations are only ~ 3.5 times stronger than that of the host star at *Spitzer*/IRAC wavelengths (see Fig. A3 for a depiction).

Our predicted ellipsoidal and gravity darkening variations are consistent with past predictions (Budaj 2011) and with the amplitude of the Zhang PLD model with second-order sinusoidal variations fitted to the $3.6 \mu\text{m}$ data collected in 2010 (we set the offset to zero as there is no significant detection of an offset in this phase curve). However, the expected ellipsoidal and gravity darkening variations are highly discrepant with the observed amplitude at $4.5 \mu\text{m}$ (see Fig. A4). Running simulations where the planet fills its Roche lobe ($R_{p,2}/R_p \approx 1.4$), our ellipsoidal variations and gravity darkening model would be able to explain the full amplitude of the $4.5 \mu\text{m}$ phase curve, but the variations remain mostly monochromatic and the model drastically over predicts the variations in the $3.6 \mu\text{m}$ phase curve.

APPENDIX D: RED NOISE TESTS

The bottom rows of Figs A5–A10 show the observed standard deviation in the residuals versus the number of data cubes binned together for each light curve made using the BINRMS routine from the MC3³ package (Cubillos et al. 2017); this allows us to test for any red noise remaining in our residuals (Winn et al. 2007; Cowan et al. 2012). These figures show that minimal red noise remains after our fiducial models have been subtracted from the data (the photometric uncertainty decays roughly as $\sqrt{N_{\text{binned}}}$). There is, however, some lower frequency noise in the 2010 $4.5 \mu\text{m}$ observations between the first eclipse and the transit that cannot be modelled by any of the three decorrelation pipelines.

APPENDIX E: NUV EVIDENCE FOR MASS LOSS

Across the NUV, WASP-12b appears to be larger than the planet’s Roche radius, implying significant mass loss (Fossati et al. 2010; Haswell et al. 2012; Nichols et al. 2015). The first *Hubble Space Telescope*, Cosmic Origins Spectrograph transit observation of WASP-12b (Fossati et al. 2010) also detected an early ingress in the NUV; this suggests the presence of a stream of gas stripped from the planet flowing in toward the star (Lai et al. 2010; Bisikalo et al. 2013b; Matsakos et al. 2015) which forms a bow shock ahead of the planet (Vidotto, Jardine & Helling 2010; Llama et al. 2011; Bisikalo et al. 2013b; Cherenkov, Bisikalo & Kaigorodov 2014; Matsakos et al. 2015; Turner et al. 2016), although the position of this shock can vary (Vidotto, Jardine & Helling 2011; Llama et al. 2013). There is also evidence for variable NUV ingress times (Haswell et al. 2012; Nichols et al. 2015) which suggests variable mass-loss rates and/or a variations in the planet–shock distance (Vidotto et al. 2011). The non-detection of stellar activity indicators from WASP-12A (Knutson, Howard & Isaacson 2010; Fossati et al. 2013) may also suggest that WASP-12b is undergoing mass loss. The final resting place of the gas stripped from WASP-12b is debated, with some suggesting an accretion disc interior to the planet’s orbit (Lai et al. 2010; Li et al. 2010) and others suggesting an extended circumstellar torus of gas with the planet embedded inside (Debrecht et al. 2018).

APPENDIX F: DISCUSSION OF VARIABILITY

To date, no *Spitzer* phase curve observation has shown variability in the phase curve offset of an exoplanet, although significant near-infrared variability has been seen for brown dwarfs and isolated

³<http://pcubillos.github.io/MC3cubed/>

planetary mass objects (Artigau et al. 2009; Radigan et al. 2012), and *Kepler* phase curves of the hot Jupiter HAT-P-7b have been reported to vary (Armstrong et al. 2016). Variability is expected for WASP-12b due to coupling between the planet’s partially ionized atmosphere and the planet’s magnetic field (Rogers 2017). The time-scale of this variability is set by the Alfvén time-scale (~ 115 d for WASP-12b assuming magnetic effects occur on the dayside where the atmosphere is dominated by atomic hydrogen; Rogers 2017; Dang et al. 2018). Variability may also arise in the presence of time-variable cloud coverage, although optically reflective clouds on the planet’s dayside were stringently rejected using *Hubble* Space Telescope Imaging Spectrograph optical eclipse spectroscopy of WASP-12b (Bell et al. 2017). Any time variability in the gas streaming from the planet could also obscure different portions of the planet over time and lead to an apparent variation in the $3.6 \mu\text{m}$ phase curve.

APPENDIX G: MODEL SELECTION

The preferred model for each phase curve was chosen to be the model with the lowest BIC, defined as

$$\text{BIC} = -2 \ln(L) + N_{\text{par}} \ln(N_{\text{dat}}),$$

where N_{par} is the number of model parameters and N_{dat} is the number of data. The log-likelihood is

$$\ln(L) = -\frac{\chi^2}{2} - N_{\text{dat}} \ln(\sigma_F) - \frac{N_{\text{dat}}}{2} \ln(2\pi)$$

where σ_F is the fitted photometric uncertainty (assumed to be constant throughout the observation) and

$$\chi^2 = \frac{\sum_i (F_{\text{obs},i} - F_{\text{model},i})^2}{\sigma_F^2}$$

is a measure of the badness-of-fit, where $F_{\text{obs},i}$ are the observed flux measurements. We adopt the threshold that models with a $\Delta\text{BIC} \leq 5$ with respect to the favoured model cannot be strongly ruled out.

This paper has been typeset from a $\text{\TeX}/\text{\LaTeX}$ file prepared by the author.